
LIKELIHOOD-FREE INFERENCE IN STATE-SPACE MODELS WITH UNKNOWN DYNAMICS

Alexander Aushev

Helsinki Institute for Information Technology
Department of Computer Science
Aalto University, Finland
alexander.aushev@aalto.fi

Thong Tran

Helsinki Institute for Information Technology
Department of Computer Science
Aalto University, Finland
thong.tran@aalto.fi

Henri Pesonen

Department of Biostatistics
University of Oslo, Norway
henri.pesonen@medisin.uio.no

Andrew Howes

School of Computer Science
University of Birmingham, UK
andrew.howes@aalto.fi

Samuel Kaski

Helsinki Institute for Information Technology
Department of Computer Science
Aalto University, Finland
Department of Computer Science
University of Manchester, UK
samuel.kaski@aalto.fi

November 3, 2021

ABSTRACT

We introduce a method for inferring and predicting latent states in the important and difficult case of state-space models where observations can only be simulated, and transition dynamics are unknown. In this setting, the likelihood of observations is not available and only synthetic observations can be generated from a black-box simulator. We propose a way of doing likelihood-free inference (LFI) of states and state prediction with a limited number of simulations. Our approach uses a multi-output Gaussian process for state inference, and a Bayesian Neural Network as a model of the transition dynamics for state prediction. We improve upon existing LFI methods for the inference task, while also accurately learning transition dynamics. The proposed method is necessary for modelling inverse problems in dynamical systems with computationally expensive simulations, as demonstrated in experiments with non-stationary user models.

1 Introduction

Likelihood-free inference (LFI) methods [1, 2] estimate parameters θ of a statistical model, given an observed measurement \mathbf{x}^* and a black-box simulator g_θ . These methods use synthetic observations $\mathbf{x}^{(i)} \sim g_\theta(\mathbf{x}|\theta)$ produced by the simulator to assist the inference without requiring an analytical formulation of the likelihood. LFI has been successfully applied to identify parameters of complex real-world systems, such as financial markets, [3–5], species populations [6–8] and cosmology models [9–11]. A special application of LFI is time-dependent systems, which can be described as a state-space model (SSM) [12, 13]. In SSMs, observed measurements $\mathbf{x}_t \in \mathbb{R}^n$ are emitted given a series of latent variables, the states $\theta_t \in \mathbb{R}^m$, as shown in Figure 1. When working with such dynamical systems, one should account not only for an observation model g_θ but also for Markovian state transition dynamics h_θ : $\theta_{t+1} \sim h_\theta(\theta_{t+1}|\theta_t)$. Modern LFI methods can be applied only to simple settings of dynamical systems (see below),

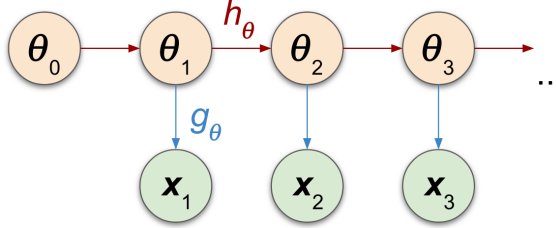


Figure 1: Graphical representation of an SSM. Latent states θ_t (orange nodes) produce observations x_t through the observation simulator g_θ (light blue) and follow the transition dynamics h_θ (dark red).

but not to cases, where h_θ is non-linear and cannot be sampled, and where the simulators are computationally expensive, as in system simulation experiments in meteorology [14, 15], simulation-based forecasting in cosmology [16, 17] or adaptive modelling of human behaviour [18, 19].

Current LFI methods for dynamical systems [20, 21] proceed by assuming some simplified form of transition dynamics in an SSM. However, unless the SSM is both linear and Gaussian, this approach leads to poor state value estimates. This issue has been addressed in a large and growing set of methods, including extended Kalman filters [22–24], GP-SSMs [25, 26], sequential Monte Carlo [27–30] and Bayes filtering [27, 31–33] methods in general. Unfortunately, when the latent states have the additional requirement of being valid simulator parameters, these methods need a tractable likelihood that is not available when the observation model is black-box. At the same time, recent works on LFI in SSMs have focused on more efficient sampling-based methods [34], generation of better matching statistics [35], and on establishing theoretical convergence guarantees [21, 36, 37]. Despite these advances, the problem of sample-efficient LFI in non-linear non-Gaussian SSMs remains unsolved.

In this paper, we introduce a method capable of likelihood-free state approximation and state prediction in discrete-time SSMs. We assume that the state transition model is unknown and can be non-linear, and that the number of samples from the observation model must be limited to be small, since simulations are computationally expensive. To solve the LFI problem in SSMs, we need to simultaneously estimate simulator parameters for observed measurements sample-efficiently, and the transition dynamics, which is required for state prediction. We propose a method, which uses a non-parametric multi-objective model for LFI of states, and a non-parametric model of transition dynamics for learning state transition dynamics. The contributions of the paper are:

- We solve the problem of state prediction in SSMs with unknown transition dynamics and limited simulation budget. We use samples from the LFI posterior approximations to accurately learn the state transition dynamics, as shown by comparisons with state-of-the-art SSM inference techniques.
- Focusing on problems where LFI has to be sample-efficient, we improve upon the current LFI methods for the state inference task by leveraging time-series information. This is done by using a multi-objective surrogate for the consecutive states and sampling from a transition dynamics model to determine where to run simulations next.
- We demonstrate that the proposed method is needed to tackle the crucial case of user modelling, where user models are non-stationary because user’s preferences and abilities change over time.

2 Background

For LFI of states, we follow the Bayesian optimization for LFI (BOLFI) approach [38], in which a Gaussian process (GP) surrogate is used for a discrepancy measure δ (e.g. Euclidean distance) between an observed measurement \mathbf{x}^* and synthetic observations $\mathbf{x}^{(i)}$. This approach assumes that if synthetic observations have a small discrepancy (smaller than a user-defined threshold ϵ), they were produced by simulator parameters that could plausibly replicate the observed measurement. In this way, the posterior can be approximated as

$$p(\boldsymbol{\theta}|\mathbf{x}^*) \propto F\left(\frac{\epsilon - \mu(\boldsymbol{\theta})}{\sqrt{\nu(\boldsymbol{\theta}) + \sigma^2}}\right) p(\boldsymbol{\theta}), \tag{1}$$

where $F(\cdot)$ is a Gaussian CDF with mean 0 and variance 1, $\mu(\boldsymbol{\theta})$ and $\nu(\boldsymbol{\theta})$ are the mean and standard deviation of the GP surrogate, and σ is a likelihood noise of the GP. Also note that the discrepancy δ depends on \mathbf{x}^* resulting in $\mu(\boldsymbol{\theta})$, $\nu(\boldsymbol{\theta})$ and σ depending on it as well, see Section 6.3 [38] for more details.

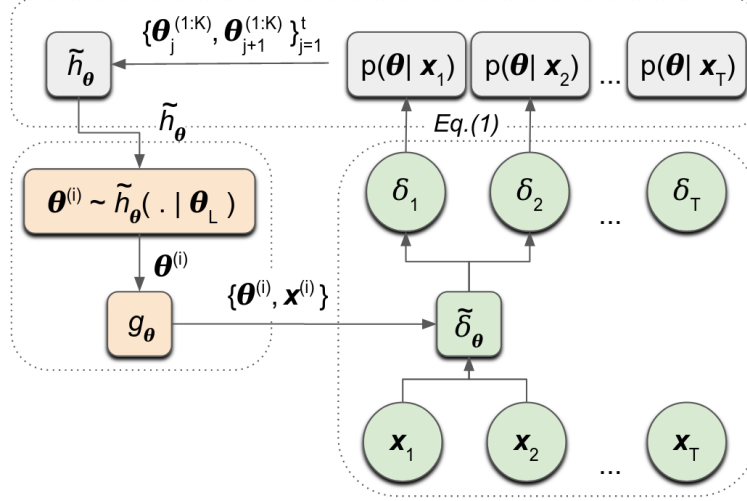


Figure 2: An overview of our approach, in which the $\tilde{\delta}_\theta$ surrogate is used for LFI and \tilde{h}_θ for the unknown transition dynamics. The $\tilde{\delta}_\theta$ models the corresponding discrepancies of several observations (green) inside a moving window (here, with the size of two), from which posteriors are extracted according to Equation (1). \tilde{h}_θ is trained with paired samples from posteriors of consecutive states (grey); its predictive samples are used as proposals (orange) for future simulations.

A main advantage of modelling the discrepancy with a GP is the uncertainty estimation. The GP predictive mean $\mu(\theta^{(i)})$ and variance $\nu(\theta^{(i)}) \equiv k(\theta^{(i)}, \theta^{(i)})$ are used to calculate the utility (e.g., Expected Improvement [39]) of sampling the objective function at the next candidate parameter value $\theta^{(i)}$. By maximizing this so-called acquisition function $\mathcal{A}^{(i)}(\cdot)$ with respect to $\theta^{(i)}$, one chooses where to run simulations next. Because BOLFI actively chooses where to run simulations, its posterior approximation requires much fewer synthetic observations than other LFI methods. However, BOLFI was not designed for SSMs, and hence, does not make use of any temporal information that is typical for SSMs to improve the quality of inference.

An alternative approach to sample-efficient LFI is sequential neural estimation (SNE), which proceeds by learning the statistical relationship between observations and parameters directly through a neural network surrogate. This surrogate does not require retraining when the observation changes, which makes SNE methods especially suitable for series of inference tasks. The SNE neural network can be used as a surrogate for the posterior, likelihood or likelihood ratio, resulting in SNPE [40–42], SNLE [43], and SNRE [44, 45] methods respectively. These SNE methods address a more difficult problem than we do, of learning a model across all possible tasks. The price is that they require significantly more simulations than BOLFI, see Section 4.3 [46].

3 Likelihood-Free Inference in State-Space Models

In this section, we introduce a multi-objective approach to LFI in SSMs, which improves sample-efficiency of existing methods by using temporal information of SSMs while also learning the unknown transition dynamics. The main elements of the solution are presented in Figure 2. To estimate state values θ_t , given \mathbf{x}_t , we employ a multi-objective surrogate $\tilde{\delta}$ for discrepancies, and then extract the LFI posterior with (1). At the same time, we form pairs of consecutive posterior samples and train a non-parametric surrogate for the state transition \tilde{h}_θ , whose predictive posterior proposes candidates for future simulations. We summarize our approach in Algorithm 1.

3.1 Multi-Objective State Inference

As an extension to BOLFI, we employ a multi-objective surrogate model for the discrepancies δ_t , thus considering multiple discrepancy objectives at the same time and leveraging information between consecutive states. More specifically, we pass discrepancies of the consecutive states to the surrogate separately, but through the use of shared parameters of the multi-objective surrogate they become associated. This approach allows using a discrepancy model of the previous state to infer the current state value, instead of simply discarding it. Moreover, it allows having a much more flexible surrogate for LFI than the traditional GP used in BOLFI. These changes do not need any additional data

Algorithm 1 Multi-Objective LFI with Transition Dynamics Model

Input: observations $\{\mathbf{x}_1, \dots, \mathbf{x}_T\}$, observation simulator g_θ , moving window size L , simulation budget b_{sim} , prior $p(\theta)$;

Output: state posterior approximation \mathcal{P} , transition dynamics model \tilde{h}_θ ;

set $\mathcal{P} = \emptyset$, initialize \tilde{h}_θ ;

get initial simulations: $\mathbf{x} = g_\theta(\theta)$, $\theta \sim p(\theta)$;

for $t = L$ **to** T **do**

 calculate discrepancies δ_i inside a moving window $i = \{t - L \dots t\}$ for all simulations;

 train $\tilde{\delta}_\theta$ on $\{\theta, \delta_i\}$;

 extract posteriors $p(\theta_i | \mathbf{x}_i)$ with Equation (1);

 update \tilde{h}_θ with pairs $\{\theta_j^{(1:K)}, \theta_{j+1}^{(1:K)}\}_{j=1}^t$, where $\theta_j^{(1:K)} \sim p(\theta_j | \mathbf{x}_j)$;

 get b_{sim} new simulations $\hat{\mathbf{x}} = g_\theta(\hat{\theta})$, $\hat{\theta} \sim \tilde{h}_\theta(\theta_{t+1} | \theta_t)$;

 add to the set $\mathbf{x} \leftarrow \hat{\mathbf{x}}$ and $\theta \leftarrow \hat{\theta}$;

 add to the set $\mathcal{P} \leftarrow p(\theta_{t-L} | \mathbf{x}_{t-L})$;

end for

to fit the surrogates, because all synthetic observations for discrepancy objectives can be shared across all state values. When we have a new observation, we simply need to recalculate the discrepancy values for all synthetic observations. Once we have a trained surrogate for discrepancy objectives, we infer state posteriors $p(\theta_t | \mathbf{x}_t)$, similarly as in BOLFI.

There is an additional challenge for adapting multi-objective surrogates in SSMs, namely high computational cost associated with considering too many objectives. SSMs can potentially have hundreds of observations, and expanding the number of considered objectives may be detrimental for the performance of the surrogate. We avoid this problem by limiting the number of objectives the surrogate can have. Instead of considering all available time-steps as objectives, we propose to consider only L recent objectives by gradually including new objectives and discarding old ones that have little impact on current states. The size of this moving window depends on how rapidly the transition dynamics change. As the size L of the window grows, the model becomes less sensitive to the noise from the dynamics, at the cost of increased computations and decreased adaptability to the most recent state transitions. Overall, the moving window reduces the number of objectives L considered at a time, making multi-objective modelling for SSMs feasible. In the Supplement, we further investigate the influence of the moving window size hyperparameter on state inference and prediction.

3.2 Learning State Transition Dynamics

While we gradually improve LFI posterior approximations $p(\theta_t | \mathbf{x}_t^*)$ by acquiring new simulations, we use empirical samples from the latest available approximations to learn a state transition model. This model should be able to train from noisy samples of LFI posterior approximations, and be flexible enough to fit arbitrary function families the dynamics may follow. In addition, it should be able to handle uncertainty associated with samples outside the training distribution, as samples from posterior approximations tend to be concentrated around local parameter space regions. For these reasons, the appropriate transition model should be Bayesian and non-parametric. Such a model would take the uncertainty associated with posterior approximations into account and be flexible enough to follow possibly non-linear transition dynamics.

We propose to train this model in an autoregressive fashion by forming a training set from paired sample points from posteriors. More specifically, we assume Markov property in the transition dynamics and use pairs of states instead of their whole trajectories. For each SSM time interval, we group consecutive state posterior samples in a training set, and expand it when new state posteriors become available. This way, the transition model does not need to be retrained when new observations present themselves and can be actively used throughout state inference for determining where to run simulations next. This can be done, by sampling the predictive posterior $p(\theta_{T+1} | \mathbf{x}_T^*)$ from the trained model \hat{h}_θ through

$$p(\theta_{T+1} | \mathbf{x}_T^*) = \int \hat{h}_\theta(\theta_{T+1} | \theta_T) p(\theta_T | \mathbf{x}_T^*) d\theta_T. \quad (2)$$

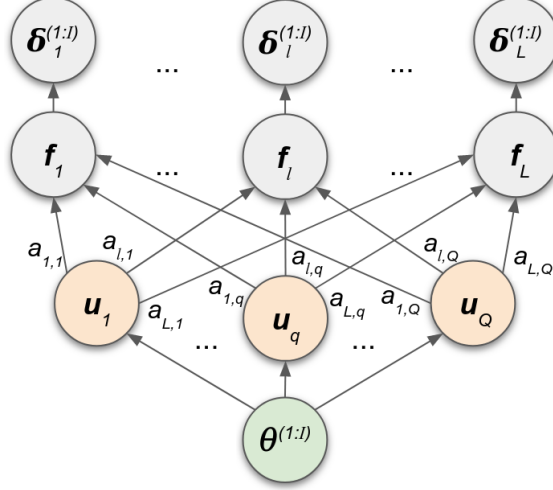


Figure 3: Graphical representation of the LMC. The discrepancy outputs $\delta_t^{(1:I)}$ are modelled as a linear combination of latent functions \mathbf{u}_q . The model shares the same parameter values $\theta^{(1:I)}$ between all objectives.

This way, the state transition model \hat{h}_θ does not inform state posteriors directly, but only provides simulation candidates for the LFI surrogate. Ultimately, accumulating more simulations improves the discrepancy surrogate for the LFI of states and, by extension, quality of posterior samples, while higher-quality posterior samples allow more accurate learning of state transition dynamics.

3.3 Computational Complexity and Model Choices

The proposed multi-objective approach to LFI requires choosing surrogate models. Here, we present the model choices for our approach, followed by a resulting complexity analysis of the Algorithm 1.

Following the requirements for the surrogates from Sections 3.1 and 3.2, we chose a linear model of coregionalization (LMC) [47] as a multi-objective surrogate for discrepancies and a Bayesian Neural Network (BNN) [48, 49] as a surrogate for state transition dynamics. LMC is one of the simplest multi-objective models that expresses each of its L outputs f_l as a linear combination $f_l(\theta^{(1:I)}) = \sum_{q=1}^Q a_{l,q} \mathbf{u}_q$, as shown in Figure 3, where the $\mathbf{u}_q \sim GP(0, k(\theta, \theta'))$ are latent GPs and the $a_{l,q}$ are linear coefficients that need to be solved. As regards BNN, it can be represented as an ensemble of neural networks, where each has its weights $w^{(h)}$ drawn from a shared, learnt probability distribution [50] with $w^{(h)} \sim \mathcal{N}(\mu^{(h)}, \log(1 + \rho^{(h)}))$, where $\rho^{(h)}$ and $\mu^{(h)}$ are the hyperparameters that require training.

Given the aforementioned model choices, the resulting computational complexity of the Algorithm 1 is dominated by three major stages: training of the multi-objective surrogate $\tilde{\delta}_\theta$, posterior extraction from discrepancy surrogates (Equation (1)) and training of the transition dynamics model \tilde{h}_θ . Starting with the cost of training $\tilde{\delta}_\theta$, it depends on the number of synthetic observations I , on the size of the moving window L and on the user-specified number M of inducing points [51] for the LMC, resulting in the complexity $\mathcal{O}(NLM^2)$, as opposed to $\mathcal{O}(NM^2)$ by traditional GPs used in BOLFI. Moving on to the posterior extraction, this stage consists of finding the appropriate ϵ , and then applying Equation (1), which is bounded by the complexity of calculating the variance of the surrogate for each of the S_1 samples from the prior, resulting in $\mathcal{O}(LM^2S_1)$. Finally, if we apply variational inference [52] to training of the transition dynamics model \tilde{h}_θ , the computational cost is linear in the number W of BNN parameters – $\mathcal{O}(WKES_2)$, where K is the overall amount of training data for \tilde{h}_θ , E is the number of epochs, and S_2 is the number of parameter samples from the posterior distribution that is required to get the distribution of outputs. Depending on the choice of hyperparameters, the computational complexity of the Algorithm 1 is bounded by either $\mathcal{O}(NLM^2)$, $\mathcal{O}(LM^2S_1)$ or $\mathcal{O}(WKES_2)$. We provide recommendations for choosing these hyperparameters in the supplement.

4 Experiments

We assess the quality of our method for state inference and prediction tasks in a series of SSM experiments, where a simulator serves as the observation model g_θ . In the experiments, our method uses the surrogate choices of LMC

and BNN, as was described in Section 3.3. We demonstrate that it can accurately learn state transition dynamics and improve upon existing LFI methods for the state inference task. Moreover, we investigate sample-efficiency of the proposed method and demonstrate its effectiveness in non-stationary user modelling case studies.

4.1 Experimental setup

We simulated time series of observations based on single sampled trajectories from true transition dynamics of five SSMs, described in Section 4.2. Our goal was to estimate the simulator parameters that likely produced these observations, and learn the model of transition dynamics for state prediction based on the sampled trajectory.

For the state inference task, we compare the quality of state estimates by our approach against other LFI methods: BOLFI [38], SNPE [40], SNLE [43], SNRE [44]. We use a fixed simulation budget for all these methods, with 20 simulations to initialize the models, and then with 2 additional simulations for each new time-step. For the SNE approaches (SNPE, SNLE, SNRE), we provided all simulations at once, since that is their intended mode of operation. As for the prediction task, we sampled trajectories from the transition model and evaluated them against trajectories from the true dynamics. We performed these experiments in SSMs with simulators that have tractable likelihoods, providing the ground-truth likelihoods to the state-of-the-art SSM inference methods GP-SSM [26, 53] and PR-SSM [54], while our method was still doing LFI. For all methods in the prediction task, we provided 50 observations, and then sampled trajectories that had the same length of 50 time-steps.

We also compared two variants of our method that differ only in the way the next simulations are sampled: LMC-BLR, where samples were taken from Bayesian linear regression (BLR) models that linearized the transition dynamics along 50 observed time-steps; and LMC-qEHVI, where a popular acquisition function for multitask BO, q-expected hypervolume improvement (qEHVI) [55], was used to provide samples. The role of these variants was to evaluate how the choice of the future simulations impacts the quality of state inference and prediction.

All models were assessed in terms of the root-mean-square error (RMSE) between the state estimates and their ground-truths. The experiments were repeated 30 times with different random seeds. Additional details on implementation of the methods and all code for replicating the experiments are provided in the Supplement.

4.2 The State-Space Models

In this section, we present two case studies with non-stationary user models and three SSMs with tractable likelihoods. In user modelling experiments, we simulated behavioural data from humans that completed a certain task in two different experiments, described in Sections 4.2.1 and 4.2.2. During the first task, the user searched for a target on a display and the search time was measured. For the second task, the user evaluated dataset embeddings for a classification problem, and the evaluation score was used as behavioural data. Our task in the experiments was to track the changing parameters of user models and learn their dynamics.

In addition to non-stationary user models, we also experimented with three models with tractable likelihoods, common in SSM literature: linear Gaussian (LG), non-linear non-Gaussian (NN) and stochastic volatility (SV) models. In the LG model, the state transition dynamics and observation model are both linear, with high observational noise. The NN model is a popular non-linear SSM [56], where each observation has two unique solutions. Lastly, we used the SV model [57], which is used for predicting volatility of asset prices in stock markets [58, 59]. The dimensionality of states in these models ranges from one to three. We provide full descriptions of these SSMs in the Supplement.

4.2.1 UMAP Parameterization

With the first non-stationary user model, we infer uniform manifold approximation and projection (UMAP) [60] parameters that best satisfy human subject’s needs. We assume that the subject uses UMAP to generate low-dimensional data representations for a classification task, and that their preferences change with time. Specifically, in the beginning, the subject does not have any prior knowledge of the dataset, so data exploration takes the priority. As they become more familiar with the data, the priority gradually shifts from exploration to maximizing classification accuracy of their model. Our hypothesis is that by modelling the change in subject’s preferences, we can anticipate the preferences and propose good UMAP parameter candidates faster to the human user.

For this experiment, the subject’s needs are simulated by an evaluation function that takes the embedding of the handwritten digit dataset [61] as an input and assigns a corresponding preference score. The evaluation function is based on the weighted sum of the density based cluster validity (DBCv) score $\mathcal{U}^{(i)}$ [62] and the c-support vector classification (SVC) [63, 64] accuracy $\mathcal{P}^{(i)}$. By regulating the weight w_t , one can prioritize data exploration $\mathcal{U}^{(i)}$ or maximization of a classification accuracy $\mathcal{P}^{(i)}$ with

$$\delta_t^{(i)} = (1 - w_t) \mathcal{U}^{(i)} + w_t \mathcal{P}^{(i)}, \quad w_t = \frac{1}{1 + e^{-0.1(t-25)}}. \quad (3)$$

We assume the subject cannot explicitly specify the ideal embedding, and hence the SSM observations \mathbf{x}_t are latent. But since the subject has the ability to evaluate embeddings with the preference score, we model the preference score $\delta_t^{(i)}$ directly as an objective. The goal is to infer the state values $\theta = \{\theta_d, \theta_{dist}, \theta_n\}$ of the UMAP parameters: the dimension of the target reduced space θ_d , an algorithmic parameter θ_{dist} that controls how densely the points packed, and the neighbourhood size θ_n to use for local metric approximation. In summary, the UMAP algorithm serves as an observation model and the transition dynamics are unknown, but implicitly regulated through (3). We use uniform priors for states throughout the experiments:

$$\theta_d \sim \text{Unif}(1, 64) \in \mathbb{Z} \quad (4)$$

$$\theta_{dist} \sim \text{Unif}(0, 0.99) \in \mathbb{R} \quad (5)$$

$$\theta_n \sim \text{Unif}(2, 200) \in \mathbb{Z}. \quad (6)$$

Details on the implementation of the UMAP algorithm and preference score are in the Supplement.

4.2.2 Eye Movement Control For Gaze-Based Selection

For the second non-stationary user model, we infer properties of human gaze in a series of simulated eye movement control trials [65, 66]. In these trials, the user model of the human searches for a target on a 2D screen by performing eye movements (saccades), based on its beliefs about the target location and information from peripheral vision. When the gaze location matches the location on the screen, the task is considered complete and a new target appears. As the human subject performs more tasks, they get weary, which results in an increasing latency between saccades θ_l . We believe that modelling the dynamics of eye movement latency will allow robust inference of the individual characteristics that are independent of weariness.

The subject needs several moves to reach the target because the actions and observations are corrupted with two noise sources: the ocular motor noise θ_{om} and the spatial noise of peripheral vision θ_s . The quantitative values for these two variables vary for each individual, while the saccade latency θ_l varies between different trial instances. We assess the performance of the subject based on total time $x \in \mathbb{R}$ it took for the gaze to reach the target,

$$x_t = \sum_e (2.7A^{(e)} + \theta_{l,t}), \quad \theta_{l,t} = 12 \log(t + 1) + 37. \quad (7)$$

Here, the x_t are SSM observations, $\theta = \{\theta_{om}, \theta_s, \theta_l\}$ are state values that need to be inferred, $A^{(e)}$ is the saccade amplitude, and e is the saccade index. The increase of the latency θ_l serves as state transition dynamics h_θ that needs to be modelled for prediction, while eye movement control task environment is considered as an observation model g_θ . To produce behavioural data, ground truth values of 0.01 and 0.09 for θ_{om} and θ_s respectively were used in the observation model. Finally, we calculate a Euclidean distance directly applied to x as a discrepancy and use the following priors for the states:

$$\theta_{om} \sim \text{Unif}(0, 0.2) \in \mathbb{R} \quad (8)$$

$$\theta_s \sim \text{Unif}(0, 0.2) \in \mathbb{R} \quad (9)$$

$$\theta_l \sim \text{Unif}(30, 60) \in \mathbb{R}, \quad (10)$$

The user model was implemented with reinforcement learning by [67]. More details on implementation can be found in the Supplement.

4.3 Results and Analysis

The results for the inference and prediction tasks are presented in Tables 1 and 2, respectively. The lower the RMSE, the better is the quality of estimation. In the inference task, LMC-based methods clearly outperformed BOLFI and SNE approaches. This indicates that considering multiple objectives at the same time was beneficial for the state

Table 1: Comparison of LFI methods (rows) in different SSMs (columns) for the state inference task. The performance was measured with 95% confidence interval (CI) of the RMSE between estimated vs ground truth state values for 50 time-steps. The best results in each column are highlighted in bold.

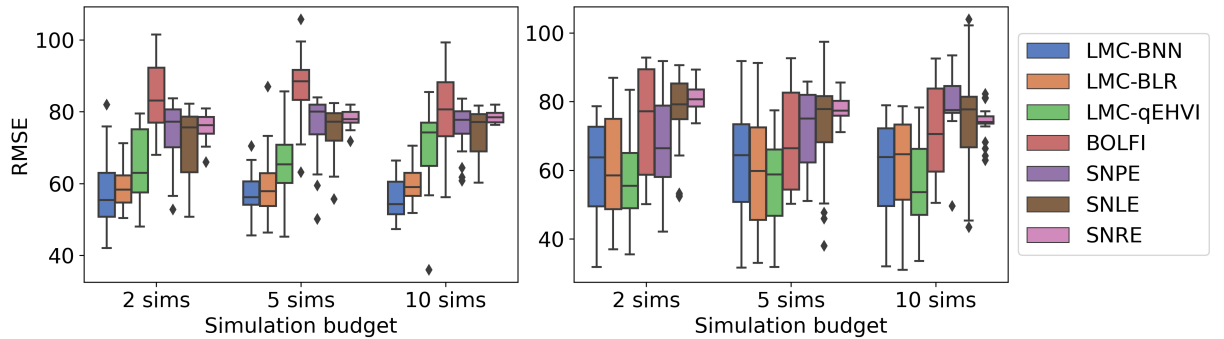
Methods	LG	NN	SV	UMAP	Gaze
LMC-BNN	1.77 ± 0.12	6.92 ± 0.51	16.14 ± 3.27	58.24 ± 3.62	58.7 ± 5.4
LMC-BLR	1.3 ± 0.1	6.86 ± 0.54	13.15 ± 3.25	59.19 ± 3.31	60.6 ± 5.8
LMC-qEHVI	1.5 ± 0.1	7.03 ± 0.55	24.4 ± 2.5	64.96 ± 3.72	56.9 ± 4.5
BOLFI	1.55 ± 0.15	7 ± 0.6	27.35 ± 3.45	84.31 ± 3.54	73.45 ± 5.75
SNPE	7.15 ± 0.65	18.2 ± 0.93	77.4 ± 3.1	74.13 ± 3.21	68.1 ± 7.8
SNLE	6 ± 0.5	10.35 ± 0.64	54.25 ± 2.45	71.45 ± 3.44	77.25 ± 4.05
SNRE	10.4 ± 1.7	17.93 ± 1.34	57.15 ± 2.35	75.85 ± 1.26	80.75 ± 1.35

Table 2: Comparison of transition dynamics models (rows) in different SSMs (columns). The performance was measured with 95% CI of the RMSE between sampled vs ground truth trajectories of length 50. The best results in each column are highlighted in bold.

Methods	LG	NN	SV	UMAP	Gaze
LMC-BNN	210 ± 4	148 ± 2	117 ± 21	1394 ± 27	1365 ± 3
LMC-BLR	64 ± 7	154 ± 4	100 ± 37	1409 ± 49	1372 ± 3
GP-SSM	284 ± 71	2204 ± 1111	3206 ± 1175	-	-
PR-SSM	253 ± 68	610 ± 510	1378 ± 740	-	-

Table 3: Time comparison of LFI methods (rows) in different SSMs (columns) for training 50 time-steps. The running time is shown in minutes along with 95% CI. The best results in each column are highlighted in bold.

Methods	LG	NN	SV	UMAP	Gaze
LMC-BNN	87.6 ± 2.6	79.2 ± 1	81 ± 2.9	171.2 ± 5	408 ± 8
LMC-BLR	82.1 ± 5.5	48.2 ± 0.8	93.5 ± 4	149.4 ± 4.5	442.5 ± 8.8
LMC-qEHVI	25.5 ± 1.5	23.9 ± 0.5	24.7 ± 0.7	116 ± 4.6	347.2 ± 7.3
BOLFI	1.1 ± 0	1 ± 0	1.7 ± 0.1	129.3 ± 11.7	369.5 ± 16.5
SNPE	0.1 ± 0	0.1 ± 0	0.4 ± 0	168.6 ± 4.4	710.9 ± 415
SNLE	119.4 ± 2.9	137.3 ± 5.8	355.3 ± 23.1	582.7 ± 23.8	1003.4 ± 92.4
SNRE	34 ± 1.5	35.4 ± 0.3	110.2 ± 6.1	309.6 ± 8.6	446.4 ± 14



(a) UMAP parameterization model

(b) Eye movement control for gaze-based selection

Figure 4: The performance of LFI methods for the state inference tasks with various simulation budgets in two non-stationary user modelling experiments. The box plots were computed from 30 repetitions with different random seeds. The horizontal line on box plots shows the median, the bar shows upper and lower quartiles, and the whiskers indicate the rest of the quartiles. The diamond points indicate outliers.

inference, and that the model actually leverages information from consecutive states without hindering the performance. Additionally, it can be seen that all LMC-based variants performed differently, which can be only attributed to how the next simulations were chosen, since the surrogate was exactly the same in all three methods. As the results show, having BNN as a model for state transition was beneficial for experiments with non-stationary user models, while having BLR was more preferable for the simpler models. This suggests that BLR is expressive enough to replicate simple transitions, but struggles with more complex ones, for which BNN was more suitable.

The comparisons with GP-SSMs and PR-SSMs for learning transition dynamics show that our method learns the accurate dynamics or, at least, relative to the SSM method baselines. The SSMs methods showed worse results than BLR and BNN approaches. This can be explained by the lack of observations for learning state transitions by the SSM methods, which also explains the high variance in the sampled trajectories from these methods. As for comparisons between BLR and BNN, BLR performs better only in LG and SV models, while BNN performs better in more complex case studies. Moreover, it should be noted that trajectory sampling from BLR is possible only by retaining all local linearizations of the dynamics, which is a far more limiting approach than having one single model. Therefore, BNN is a more preferable transition dynamics model.

The empirical time costs for running the LFI methods are shown in Table 3. It can be seen that the SNPE method was the fastest for the computationally cheap simulators (of SSMs with tractable likelihoods), while the LMC-qEHVI required the least amount of time for the non-stationary user models. This is expected, since the SNEs learn the model only once, and then simply use it for all observations, which is suitable for the computationally cheap simulations with simple LFI solutions. However, for the non-stationary user models, where there are no closed-form likelihoods available, learning a single model actually requires much more time. To summarize, the LMC variants are clearly preferable for the computationally heavy simulators, which dominate the cost of training a transition dynamics model and a multi-objective surrogate.

Finally, Figure 4 shows how the performance of the LFI models changes with different simulation budgets: 2, 5, and 10 simulations per each time-step. As expected, in general, all methods improved their performance with increased budgets. However, there is little difference in how these methods compare with respect to each other. This indicates that the results are not sensitive to the precise simulation budget.

In all experiments, we attribute the success of the proposed LMC-BNN method to a more flexible multi-output surrogate, and a more efficient way of choosing simulation candidates. The LMC allows multi-fidelity modelling and leveraging information from multiple consecutive time-steps, unlike standard GPs. At the same time, samples from the transition model provide better candidates for simulations than the alternatives. The flexible surrogate along with adaptive acquisition make our method particularly suitable for online settings, where only a handful of samples are allowed per time-step.

5 Discussion

We proposed an approach for state inference and prediction in the challenging SSM setting, where the transition dynamics are unknown and observations can only be simulated. Importantly, our model of transition dynamics was obtained with few simulations, making it suitable for cases with computationally expensive simulators. This is important because typically sample-efficient LFI approaches discard any temporal information from observed time-series, and cannot do state prediction, which is necessary for choosing the next simulations when simulation budget is limited. We proposed a solution for both these challenges: we use a multi-objective surrogate model for the discrepancy measure between observed and synthetic data, which connects the consecutive states through shared parameters, and we train an additional surrogate for state transitions with samples from LFI state posteriors. Additionally, our method does not restrict the family of admissible solutions for the state transitions to be linear or Gaussian, unlike existing LFI methods for SSMs [34, 37], making it more widely applicable.

Although our method uses a more flexible surrogate for LFI, we demonstrated that it requires neither additional data nor significantly more training time than traditionally used GP surrogates. We reached the sample-efficiency goal by sharing synthetic observations across all discrepancy objectives, allowing the method to use the same simulations an indefinite amount of times. As for the decreased training time, we proposed a moving window approach that allowed the surrogate to focus only on a few recent SSM time-steps at a time. In conclusion, having a more flexible surrogate improved state inference and provided better samples from state posteriors for learning the unknown dynamics.

The main limitation of our approach is that the proposed transition dynamics model does not account for long-term state dependencies. Our state transition surrogate considers only the most recent state as an input, assuming the Markov property, and therefore cannot forecast far into the future. The resulting predictions have very low variance and have a

tendency to converge to similar values, which can be explained by training only on a single trajectory. This limits our method to cases where observations are highly informative.

Acknowledgements

This work was supported by the Academy of Finland (Flagship programme: Finnish Center for Artificial Intelligence FCAI; grants 328400, 319264, 292334) and UKRI Turing AI World-Leading Researcher Fellowship EP/W002973/1. HP was also supported by European Research Council grant 742158 (SCARABEE, Scalable inference algorithms for Bayesian evolutionary epidemiology). Computational resources were provided by the Aalto Science-IT Project.

Code Availability

All code is available through <https://github.com/alexaushev/LFI-in-SSMs-with-Unknown-Dynamics>

References

- [1] Scott A Sisson, Yanan Fan, and Mark Beaumont. *Handbook of approximate Bayesian computation*. CRC Press, 2018.
- [2] Mikael Sunnåker, Alberto Giovanni Busetto, Elina Numminen, Jukka Corander, Matthieu Foll, and Christophe Dessimoz. Approximate Bayesian computation. *PLoS Comput Biol*, 9(1):e1002803, 2013.
- [3] Gareth W Peters, Scott A Sisson, and Yanan Fan. Likelihood-free Bayesian inference for α -stable models. *Computational Statistics & Data Analysis*, 56(11):3743–3756, 2012.
- [4] Simon Barthelmé and Nicolas Chopin. Expectation propagation for likelihood-free inference. *Journal of the American Statistical Association*, 109(505):315–333, 2014.
- [5] Victor M-H Ong, David J Nott, Minh-Ngoc Tran, Scott A Sisson, and Christopher C Drovandi. Likelihood-free inference in high dimensions with synthetic likelihood. *Computational Statistics & Data Analysis*, 128:271–291, 2018.
- [6] Mark A Beaumont. Approximate Bayesian computation in evolution and ecology. *Annual review of ecology, evolution, and systematics*, 41:379–406, 2010.
- [7] Giorgio Bertorelle, Andrea Benazzo, and S Mona. ABC as a flexible framework to estimate demography over space and time: some cons, many pros. *Molecular ecology*, 19(13):2609–2625, 2010.
- [8] Mark A Beaumont, Wenyang Zhang, and David J Balding. Approximate Bayesian computation in population genetics. *Genetics*, 162(4):2025–2035, 2002.
- [9] Chad M Schafer and Peter E Freeman. Likelihood-free inference in cosmology: Potential for the estimation of luminosity functions. In *Statistical Challenges in Modern Astronomy V*, pages 3–19. Springer, 2012.
- [10] Justin Alsing, Benjamin Wandelt, and Stephen Feeney. Massive optimal data compression and density estimation for scalable, likelihood-free inference in cosmology. *Monthly Notices of the Royal Astronomical Society*, 477(3):2874–2885, 2018.
- [11] Niall Jeffrey, Justin Alsing, and François Lanusse. Likelihood-free inference with neural compression of DES SV weak lensing map statistics. *Monthly Notices of the Royal Astronomical Society*, 501(1):954–969, 2021.
- [12] Daphne Koller and Nir Friedman. *Probabilistic graphical models: principles and techniques*. MIT press, 2009.
- [13] Rudolf Emil Kalman et al. Contributions to the theory of optimal control. *Boletín de la Sociedad Matemática*, 5(2):102–119, 1960.
- [14] Xubin Zeng, Robert Atlas, Ronald J Birk, Frederick H Carr, Matthew J Carrier, Lidia Cucurull, William H Hooke, Eugenia Kalnay, Raghu Murtugudde, Derek J Posselt, et al. Use of observing system simulation experiments in the United States. *Bulletin of the American Meteorological Society*, 101(8):E1427–E1438, 2020.
- [15] Ronald M Errico, Runhua Yang, Nikki C Privé, King-Sheng Tai, Ricardo Todling, Meta E Sienkiewicz, and Jing Guo. Development and validation of observing-system simulation experiments at NASA’s global modeling and assimilation office. *Quarterly Journal of the Royal Meteorological Society*, 139(674):1162–1178, 2013.
- [16] Johannes U Lange, Frank C van den Bosch, Andrew R Zentner, Kuan Wang, Andrew P Hearin, and Hong Guo. Cosmological evidence modelling: a new simulation-based approach to constrain cosmology on non-linear scales. *Monthly Notices of the Royal Astronomical Society*, 490(2):1870–1878, 2019.

- [17] Siyu He, Yin Li, Yu Feng, Shirley Ho, Siamak Ravanbakhsh, Wei Chen, and Barnabás Póczos. Learning to predict the cosmological structure formation. *Proceedings of the National Academy of Sciences*, 116(28):13825–13832, 2019.
- [18] Theodosios Georgiou and Yiannis Demiris. Adaptive user modelling in car racing games using behavioural and physiological data. *User Modeling and User-Adapted Interaction*, 27(2):267–311, 2017.
- [19] Olivier Gimenez, Vivien Rossi, Rémi Choquet, Camille Dehais, Blaise Doris, Hubert Varella, Jean-Pierre Vila, and Roger Pradel. State-space modelling of data on marked individuals. *Ecological modelling*, 206(3-4):431–438, 2007.
- [20] Tina Toni, David Welch, Natalja Strelkowa, Andreas Ipsen, and Michael PH Stumpf. Approximate Bayesian computation scheme for parameter inference and model selection in dynamical systems. *Journal of the Royal Society Interface*, 6(31):187–202, 2009.
- [21] Thomas A Dean, Sumeetpal S Singh, Ajay Jasra, and Gareth W Peters. Parameter estimation for hidden Markov models with intractable likelihoods. *Scandinavian Journal of Statistics*, 41(4):970–987, 2014.
- [22] Emrah Zerdali and Murat Barut. The comparisons of optimized extended Kalman filters for speed-sensorless control of induction motors. *IEEE Transactions on industrial electronics*, 64(6):4340–4351, 2017.
- [23] Brian DO Anderson and John B Moore. *Optimal filtering*. Courier Corporation, 2012.
- [24] Masaru Hoshiya and Etsuro Saito. Structural identification by extended Kalman filter. *Journal of engineering mechanics*, 110(12):1757–1770, 1984.
- [25] Silvan Melchior, Sebastian Curi, Felix Berkenkamp, and Andreas Krause. Structured variational inference in unstable Gaussian process state space models. *arXiv preprint arXiv:1907.07035*, 2019.
- [26] Roger Frigola, Yutian Chen, and Carl Edward Rasmussen. Variational Gaussian process state-space models. *Advances in neural information processing systems*, 27:3680–3688, 2014.
- [27] Arnaud Doucet, Nando De Freitas, Neil James Gordon, et al. *Sequential Monte Carlo methods in practice*, volume 1. Springer, 2001.
- [28] Sinan Yıldırım, Sumeetpal S Singh, Thomas Dean, and Ajay Jasra. Parameter estimation in hidden Markov models with intractable likelihoods using sequential Monte Carlo. *Journal of Computational and Graphical Statistics*, 24(3):846–865, 2015.
- [29] Adrian Smith. *Sequential Monte Carlo methods in practice*. Springer Science & Business Media, 2013.
- [30] François Septier, Gareth W Peters, and Ido Nevat. Bayesian filtering with intractable likelihood using sequential MCMC. In *2013 IEEE International Conference on Acoustics, Speech and Signal Processing*, pages 6313–6317. IEEE, 2013.
- [31] Maximilian Karl, Maximilian Soelch, Justin Bayer, and Patrick Van der Smagt. Deep variational Bayes filters: Unsupervised learning of state space models from raw data. *arXiv preprint arXiv:1605.06432*, 2016.
- [32] M Sanjeev Arulampalam, Simon Maskell, Neil Gordon, and Tim Clapp. A tutorial on particle filters for online nonlinear/non-Gaussian Bayesian tracking. *IEEE Transactions on signal processing*, 50(2):174–188, 2002.
- [33] Vaclav Smidl and Anthony Quinn. Variational Bayesian filtering. *IEEE Transactions on Signal Processing*, 56(10):5020–5030, 2008.
- [34] Ajay Jasra, Sumeetpal S Singh, James S Martin, and Emma McCoy. Filtering via approximate Bayesian computation. *Statistics and Computing*, 22(6):1223–1237, 2012.
- [35] Gael M Martin, Brendan PM McCabe, David T Frazier, Worapree Maneesoonthorn, and Christian P Robert. Auxiliary likelihood-based approximate Bayesian computation in state space models. *Journal of Computational and Graphical Statistics*, 28(3):508–522, 2019.
- [36] Laurent E Calvet and Veronika Czellar. Accurate methods for approximate Bayesian computation filtering. *Journal of Financial Econometrics*, 13(4):798–838, 2015.
- [37] James S Martin, Ajay Jasra, Sumeetpal S Singh, Nick Whiteley, Pierre Del Moral, and Emma McCoy. Approximate Bayesian computation for smoothing. *Stochastic Analysis and Applications*, 32(3):397–420, 2014.
- [38] Michael U Gutmann and Jukka Corander. Bayesian optimization for likelihood-free inference of simulator-based statistical models. *The Journal of Machine Learning Research*, 17(1):4256–4302, 2016.
- [39] Eric Brochu, Vlad M Cora, and Nando De Freitas. A tutorial on Bayesian optimization of expensive cost functions, with application to active user modeling and hierarchical reinforcement learning. *arXiv preprint arXiv:1012.2599*, 2010.

- [40] George Papamakarios and Iain Murray. Fast ε -free inference of simulation models with Bayesian conditional density estimation. In *Advances in neural information processing systems*, pages 1028–1036, 2016.
- [41] Pedro Goncalves, Jan-Matthis Lueckmann, Giacomo Bassetto, Kaan Oecal, Marcel Nonnenmacher, and Jakob H Macke. Flexible statistical inference for mechanistic models of neural dynamics. In *Bonn Brain 3 Conference 2018, Bonn, Germany*, 2018.
- [42] David Greenberg, Marcel Nonnenmacher, and Jakob Macke. Automatic posterior transformation for likelihood-free inference. In *International Conference on Machine Learning*, pages 2404–2414. PMLR, 2019.
- [43] George Papamakarios, David Sterratt, and Iain Murray. Sequential neural likelihood: Fast likelihood-free inference with autoregressive flows. In *The 22nd International Conference on Artificial Intelligence and Statistics*, pages 837–848. PMLR, 2019.
- [44] Conor Durkan, Iain Murray, and George Papamakarios. On contrastive learning for likelihood-free inference. In *International Conference on Machine Learning*, pages 2771–2781. PMLR, 2020.
- [45] Joeri Hermans, Volodimir Begy, and Gilles Louppe. Likelihood-free MCMC with amortized approximate ratio estimators. In *International Conference on Machine Learning*, pages 4239–4248. PMLR, 2020.
- [46] Alexander Aushev, Henri Pesonen, Markus Heinonen, Jukka Corander, and Samuel Kaski. Likelihood-free inference with deep Gaussian processes. *arXiv preprint arXiv:2006.10571*, 2020.
- [47] Thomas R Fanshawe and Peter J Diggle. Bivariate geostatistical modelling: a review and an application to spatial variation in radon concentrations. *Environmental and ecological statistics*, 19(2):139–160, 2012.
- [48] Igor Kononenko. Bayesian neural networks. *Biological Cybernetics*, 61(5):361–370, 1989.
- [49] Piero Esposito. BLiTz - Bayesian layers in Torch zoo (a Bayesian deep learning library for torch). <https://github.com/piEsposito/blitz-bayesian-deep-learning/>, 2020.
- [50] Charles Blundell, Julien Cornebise, Koray Kavukcuoglu, and Daan Wierstra. Weight uncertainty in neural network. In *International Conference on Machine Learning*, pages 1613–1622. PMLR, 2015.
- [51] Mauricio A Alvarez and Neil D Lawrence. Computationally efficient convolved multiple output Gaussian processes. *The Journal of Machine Learning Research*, 12:1459–1500, 2011.
- [52] Cheng Zhang, Judith Bütepage, Hedvig Kjellström, and Stephan Mandt. Advances in variational inference. *IEEE transactions on pattern analysis and machine intelligence*, 41(8):2008–2026, 2018.
- [53] Alessandro Davide Ialongo, Mark Van Der Wilk, James Hensman, and Carl Edward Rasmussen. Overcoming mean-field approximations in recurrent Gaussian process models. *arXiv preprint arXiv:1906.05828*, 2019.
- [54] Andreas Doerr, Christian Daniel, Martin Schiegg, Duy Nguyen-Tuong, Stefan Schaal, Marc Toussaint, and Sebastian Trimpe. Probabilistic recurrent state-space models. *arXiv preprint arXiv:1801.10395*, 2018.
- [55] Samuel Daulton, Maximilian Balandat, and Eytan Bakshy. Differentiable expected hypervolume improvement for parallel multi-objective Bayesian optimization. *arXiv preprint arXiv:2006.05078*, 2020.
- [56] Genshiro Kitagawa. Monte Carlo filter and smoother for non-Gaussian nonlinear state space models. *Journal of computational and graphical statistics*, 5(1):1–25, 1996.
- [57] Ole E Barndorff-Nielsen and Neil Shephard. Econometric analysis of realized volatility and its use in estimating stochastic volatility models. *Journal of the Royal Statistical Society: Series B (Statistical Methodology)*, 64(2): 253–280, 2002.
- [58] Stephen J Taylor. Modeling stochastic volatility: A review and comparative study. *Mathematical finance*, 4(2): 183–204, 1994.
- [59] Neil Shephard. Statistical aspects of ARCH and stochastic volatility. *Monographs on Statistics and Applied Probability*, 65:1–68, 1996.
- [60] Leland McInnes, John Healy, and James Melville. UMAP: Uniform manifold approximation and projection for dimension reduction. *arXiv preprint arXiv:1802.03426*, 2018.
- [61] Ethem Alpaydin and Cenk Kaynak. Cascading classifiers. *Kybernetika*, 34(4):369–374, 1998.
- [62] Davoud Moulavi, Pablo A Jaskowiak, Ricardo JGB Campello, Arthur Zimek, and Jörg Sander. Density-based clustering validation. In *Proceedings of the 2014 SIAM international conference on data mining*, pages 839–847. SIAM, 2014.
- [63] Bernhard E Boser, Isabelle M Guyon, and Vladimir N Vapnik. A training algorithm for optimal margin classifiers. In *Proceedings of the fifth annual workshop on Computational learning theory*, pages 144–152, 1992.
- [64] Corinna Cortes and Vladimir Vapnik. Support-vector networks. *Machine learning*, 20(3):273–297, 1995.

- [65] Immo Schuetz, T Scott Murdison, Kevin J MacKenzie, and Marina Zannoli. An explanation of Fitts' law-like performance in gaze-based selection tasks using a psychophysics approach. In *Proceedings of the 2019 CHI Conference on Human Factors in Computing Systems*, pages 1–13, 2019.
- [66] Xinyong Zhang, Xiangshi Ren, and Hongbin Zha. Modeling dwell-based eye pointing target acquisition. In *Proceedings of the SIGCHI Conference on Human Factors in Computing Systems*, pages 2083–2092, 2010.
- [67] Xiuli Chen, Aditya Acharya, and Antti Oulasvirta. An adaptive model of gaze-based selection. In *CHI Conference on Human Factors in Computing Systems (CHI'21)*. Association for Computing Machinery, 2021.
- [68] John Schulman, Filip Wolski, Prafulla Dhariwal, Alec Radford, and Oleg Klimov. Proximal policy optimization algorithms. *arXiv preprint arXiv:1707.06347*, 2017.
- [69] Antonin Raffin, Ashley Hill, Maximilian Ernestus, Adam Gleave, Anssi Kanervisto, and Noah Dormann. Stable baselines3. <https://github.com/DLR-RM/stable-baselines3>, 2019.
- [70] Greg Brockman, Vicki Cheung, Ludwig Pettersson, Jonas Schneider, John Schulman, Jie Tang, and Wojciech Zaremba. OpenAI gym, 2016.
- [71] David W Scott. *Multivariate density estimation: theory, practice, and visualization*. John Wiley & Sons, 2015.
- [72] Leland McInnes, John Healy, and Steve Astels. hdbscan: Hierarchical density based clustering. *The Journal of Open Source Software*, 2(11), mar 2017. doi: 10.21105/joss.00205. URL <https://doi.org/10.21105%2Fjoss.00205>.
- [73] Ricardo JGB Campello, Davoud Moulavi, and Jörg Sander. Density-based clustering based on hierarchical density estimates. In *Pacific-Asia conference on knowledge discovery and data mining*, pages 160–172. Springer, 2013.
- [74] F. Pedregosa, G. Varoquaux, A. Gramfort, V. Michel, B. Thirion, O. Grisel, M. Blondel, P. Prettenhofer, R. Weiss, V. Dubourg, J. Vanderplas, A. Passos, D. Cournapeau, M. Brucher, M. Perrot, and E. Duchesnay. Scikit-learn: Machine learning in Python. *Journal of Machine Learning Research*, 12:2825–2830, 2011.
- [75] Leland McInnes, John Healy, Nathaniel Saul, and Lukas Grossberger. UMAP: Uniform manifold approximation and projection. *The Journal of Open Source Software*, 3(29):861, 2018.
- [76] Jarno Lintusaari, Henri Vuollekoski, Antti Kangasrääsiö, Kusti Skytén, Marko Järvenpää, Pekka Marttinen, Michael U. Gutmann, Aki Vehtari, Jukka Corander, and Samuel Kaski. ELFI: Engine for likelihood-free inference. *Journal of Machine Learning Research*, 19(16):1–7, 2018. URL <http://jmlr.org/papers/v19/17-374.html>.
- [77] GPy. GPy: A gaussian process framework in python. <http://github.com/SheffieldML/GPy>, since 2012.
- [78] Neculai Andrei. Scaled conjugate gradient algorithms for unconstrained optimization. *Computational Optimization and Applications*, 38(3):401–416, 2007.
- [79] Niranjn Srinivas, Andreas Krause, Sham M Kakade, and Matthias Seeger. Gaussian process optimization in the bandit setting: No regret and experimental design. *arXiv preprint arXiv:0912.3995*, 2009.
- [80] Richard H Byrd, Peihuang Lu, Jorge Nocedal, and Ciyou Zhu. A limited memory algorithm for bound constrained optimization. *SIAM Journal on scientific computing*, 16(5):1190–1208, 1995.
- [81] Maximilian Balandat, Brian Karrer, Daniel R. Jiang, Samuel Daulton, Benjamin Letham, Andrew Gordon Wilson, and Eytan Bakshy. BoTorch: a framework for efficient Monte-Carlo Bayesian optimization. In *Advances in Neural Information Processing Systems 33*, 2020. URL <https://proceedings.neurips.cc/paper/2020/hash/f5b1b89d98b7286673128a5fb112cb9a-Abstract.html>.
- [82] Adam Paszke, Sam Gross, Francisco Massa, Adam Lerer, James Bradbury, Gregory Chanan, Trevor Killeen, Zeming Lin, Natalia Gimelshein, Luca Antiga, et al. PyTorch: an imperative style, high-performance deep learning library. *arXiv preprint arXiv:1912.01703*, 2019.
- [83] Russel E Caflisch et al. Monte Carlo and quasi-Monte Carlo methods. *Acta numerica*, 1998:1–49, 1998.
- [84] Art B Owen. Scrambling Sobol' and Niederreiter-Xing points. *Journal of complexity*, 14(4):466–489, 1998.
- [85] James T Wilson, Frank Hutter, and Marc Peter Deisenroth. Maximizing acquisition functions for Bayesian optimization. *arXiv preprint arXiv:1805.10196*, 2018.
- [86] Ilya Sutskever, James Martens, George Dahl, and Geoffrey Hinton. On the importance of initialization and momentum in deep learning. In *International conference on machine learning*, pages 1139–1147. PMLR, 2013.
- [87] In Jae Myung. Tutorial on maximum likelihood estimation. *Journal of mathematical Psychology*, 47(1):90–100, 2003.

- [88] John Salvatier, Thomas V Wiecki, and Christopher Fonnesbeck. Probabilistic programming in Python using PyMC3. *PeerJ Computer Science*, 2:e55, 2016.
- [89] Matthew D Hoffman and Andrew Gelman. The No-U-Turn sampler: adaptively setting path lengths in Hamiltonian Monte Carlo. *J. Mach. Learn. Res.*, 15(1):1593–1623, 2014.
- [90] Alvaro Tejero-Cantero, Jan Boelts, Michael Deistler, Jan-Matthis Lueckmann, Conor Durkan, Pedro J. Gonçalves, David S. Greenberg, and Jakob H. Macke. sbi: A toolkit for simulation-based inference. *Journal of Open Source Software*, 5(52):2505, 2020. doi: 10.21105/joss.02505. URL <https://doi.org/10.21105/joss.02505>.
- [91] Kaiming He, Xiangyu Zhang, Shaoqing Ren, and Jian Sun. Deep residual learning for image recognition. In *Proceedings of the IEEE conference on computer vision and pattern recognition*, pages 770–778, 2016.

Table 4: Comparison of LFI methods (rows) in different SSMs (columns) for the state inference task with different moving window lengths (a number in parentheses). The performance was measured with 95% confidence interval (CI) of the RMSE between estimated vs ground truth state values for 50 time-steps. The best results in each column are highlighted in bold.

Methods	LG	NN	SV	UMAP	Gaze
LMC-BNN (2)	1.77 \pm 0.12	6.92 \pm 0.51	16.14 \pm 3.27	58.24 \pm 3.62	58.7 \pm 5.4
LMC-BNN (3)	1.78 \pm 0.12	6.95 \pm 0.53	15.86 \pm 2.6	56.99 \pm 2.68	59.45 \pm 5.02
LMC-BNN (5)	1.76 \pm 0.11	6.84 \pm 0.49	17.6 \pm 2.69	58.89 \pm 2.9	60.26 \pm 5.31
LMC-BLR (2)	1.3 \pm 0.1	6.86 \pm 0.54	13.15 \pm 3.25	59.19 \pm 3.31	60.6 \pm 5.8
LMC-BLR (3)	1.76 \pm 0.13	6.84 \pm 0.65	12.14 \pm 2.46	61.68 \pm 4.22	60.49 \pm 5.01
LMC-BLR (5)	1.8 \pm 0.16	7.12 \pm 0.54	12.83 \pm 2.78	61.8 \pm 5	60.35 \pm 5.29
LMC-qEHVI (2)	1.5 \pm 0.1	7.03 \pm 0.55	24.4 \pm 2.5	64.96 \pm 3.72	56.9 \pm 4.5
LMC-qEHVI (3)	1.47 \pm 0.1	7.37 \pm 0.53	26.02 \pm 2.5	68.75 \pm 4.13	61.68 \pm 4.85
LMC-qEHVI (5)	1.41 \pm 0.07	6.92 \pm 0.64	26.64 \pm 2.7	67.42 \pm 2.92	60.76 \pm 4.74

Table 5: Comparison of transition dynamics models (rows) in different SSMs (columns) with different moving window lengths (a number in parentheses). The performance was measured with 95% CI of the RMSE between sampled vs ground truth trajectories of length 50. The best results in each column are highlighted in bold.

Methods	LG	NN	SV	UMAP	Gaze
LMC-BNN (2)	210 \pm 4	148 \pm 2	117 \pm 21	1394 \pm 27	1365 \pm 3
LMC-BNN (3)	209 \pm 3	147 \pm 2	123 \pm 25	1408 \pm 28	1367 \pm 2
LMC-BNN (5)	208 \pm 3	147 \pm 1	134 \pm 27	1416 \pm 36	1366 \pm 2
LMC-BLR (2)	64 \pm 7	154 \pm 4	100 \pm 37	1409 \pm 49	1372 \pm 3
LMC-BLR (3)	197 \pm 6	153 \pm 4	79 \pm 22	1387 \pm 56	1367.2
LMC-BLR (5)	197 \pm 5	150 \pm 2	84 \pm 22	1404 \pm 67	1370 \pm 5

A Moving Window Experiments

We summarize the performance of our multi-objective LFI approach with various moving window lengths in Tables 4, 5 and 6, where the moving window size is shown in parentheses after the method’s name. The main finding of these experiments is that including only two objectives inside the moving window is sufficient to get the most performance benefits, while having more objectives leads to increased computation time and inconsistent performance results. The increase in computation (Table 6) is evident from the complexity analysis in Section 3.3, as it makes the multi-objective surrogate training time to grow linearly. As for the inconsistent performance, the results become worse when transition dynamics have a rapid change rate, which makes the consequent objectives dissimilar and, hence, multi-objective modelling more difficult. For example, LMC-BNN and LMC-qEHVI improved for the LG and NN cases (see Tables 4, 5), which had mostly smooth trajectories, but struggled with the SV case, which had occasional erratic transitions, as shown in Figure 5c. These results indicate that one should choose the moving window size according to the transition dynamics’ change rate, which is difficult to determine when dynamics are unknown. Therefore, because any supposed improvements of having bigger moving windows are small and computationally more costly, when dealing with unknown dynamics we recommend setting moving window size to two objectives.

It is also noteworthy to mention how different acquisition methods are impacted by having additional objectives. Starting with LMC-BNNs, with more objectives, the transition dynamics model gets samples from more frequently updated state posterior approximations, since each objective stays longer inside a moving window and their corresponding posteriors are updated every time the window moves. This is beneficial for simple transition dynamics where the multi-objective surrogate maintains a good fit with high number of objectives (e.g. LG, NN), but not for the SV case, where the surrogate struggles with modelling a lot of objectives. At the same time, these performance losses and gains remain negligible. The next acquisition method, LMC-qEHVI, is not impacted by the quality of the extracted posteriors. Instead, it prioritizes optimization of objectives inside the moving window without taking into the account future states. Specifically, it works only when future objectives are very similar to the current ones, and completely fails when transition dynamics have erratic behaviour (as in SV, UMAP and Gaze). Lastly, the BLR acquisition linearizes the transition dynamics locally and when this locality increases by including more objectives, the considered locality becomes less and less linear. As a result, increasing the moving window size hinders the performance of the LMC-BLR in all cases. In conclusion, small window size for all three methods is preferable.

Table 6: Time comparison of LFI methods (rows) in different SSMs (columns) with different moving window lengths (a number in parentheses) for training 50 time-steps. The running time is shown in minutes along with 95% CI. The best results in each column are highlighted in bold.

Methods	LG	NN	SV	UMAP	Gaze
LMC-BNN (2)	87.6 ± 2.6	79.2 ± 1	81 ± 2.9	171.2 ± 5	408 ± 8
LMC-BNN (3)	105.8 ± 5.8	96.8 ± 2	84.9 ± 5.7	201.4 ± 6.2	457.9 ± 6.4
LMC-BNN (5)	93.8 ± 2.2	97.3 ± 2.1	102.4 ± 3.6	198.2 ± 6.1	434.4 ± 8.1
LMC-BLR (2)	82.1 ± 5.5	48.2 ± 0.8	93.5 ± 4	149.4 ± 4.5	442.5 ± 8.8
LMC-BLR (3)	82.9 ± 1.6	58.5 ± 4.1	112.2 ± 1.4	189.5 ± 7.5	496.7 ± 13.2
LMC-BLR (5)	64 ± 1.8	62.8 ± 2.7	111.6 ± 2.2	190.3 ± 6.4	513.5 ± 11.5
LMC-qEHVI (2)	25.5 ± 1.5	23.9 ± 0.5	24.7 ± 0.7	116 ± 4.6	347.2 ± 7.3
LMC-qEHVI (3)	24.7 ± 1.5	27.7 ± 0.9	25.4 ± 1	159 ± 6	340.2 ± 7.1
LMC-qEHVI (5)	28.6 ± 0.8	41.3 ± 18.3	31.7 ± 0.4	141.6 ± 7.6	394.5 ± 10.1

B The State-Space Models with Tractable Likelihoods

In this section, we present details on the three SSMs with tractable likelihoods that were used to assess the quality of state transition models in the experiments. For all three SSMs, we define transition dynamics and an observation model along with priors for LFI. As observations, we used datasets of 10 points, and their mean and standard deviation as summary statistics. The objective in Bayesian Optimization (BO) was the logarithm of Euclidean distance between the observed and simulated summary statistics.

Linear Gaussian (LG). In the LG model, state transition dynamics (Figure 5a) and an observation model are both linear

$$\theta_t = 0.95 \times \theta_{t-1} + v_t, \quad x_t = \theta_t + w_t, \quad (11)$$

with added Gaussian noise $v_t \sim \mathcal{N}(0, 1^2)$ and $w_t \sim \mathcal{N}(0, 10^2)$. The initial state value for the transition dynamics is $\theta_0 = 100$. The prior for the state values is $\theta \sim \text{Unif}(0, 15) \in \mathbb{R}$.

Non-linear non-Gaussian (NN). The NN model is a popular non-linear SSM [56], where the transition dynamics (Figure 5b) and observation model are

$$\theta_{h,t} = \frac{\theta_{h,t-1}}{2} + 25 \frac{\theta_{h,t-1}}{\theta_{h,t-1}^2 + 1} + 8 \cos(1.2t) + v_t, \quad x_t = \frac{\theta_{h,t}^2}{20} + w_t, \quad (12)$$

with added Gaussian noise $v_t \sim \mathcal{N}(0, 10)$ and $w_t \sim \mathcal{N}(0, 10)$. The initial state value for the noise standard deviation $\theta_{h,0}$ is 0 with the prior $\theta_h \sim \text{Unif}(-30, 30) \in \mathbb{R}$.

Stochastic volatility (SV) models are widely used for predicting volatility of asset prices [58, 59]. Here, we use the model by [57] that specifies transition dynamics (Figure 5c) of volatility θ_v as

$$\theta_{v,t+1} = (z_t - z_{t+1} + \sum_{j=1}^k e_j), \quad z_{t+1} = \exp(-\lambda)z_t + \sum_{j=1}^k \exp\{-\lambda(t+1-c_j)\}e_j, \quad (13)$$

with $c_{1:k} \sim \text{Unif}(t, t+1)$, $e_{1:k} \sim \text{Expon}(0.5/0.25^2)$ and $\lambda = 0.01$. The random increases of volatility are regulated by the Poisson distributed variable $k \sim \text{Poisson}(0.5\lambda^2/0.25^2)$. The observation model for the log-return of an asset $x_t \in \mathbb{R}$ follows

$$x_t = \theta_\mu + \theta_\beta \theta_{v,t} + (\theta_{v,t}^{0.5} + 10^{-5})\varepsilon_t, \quad (14)$$

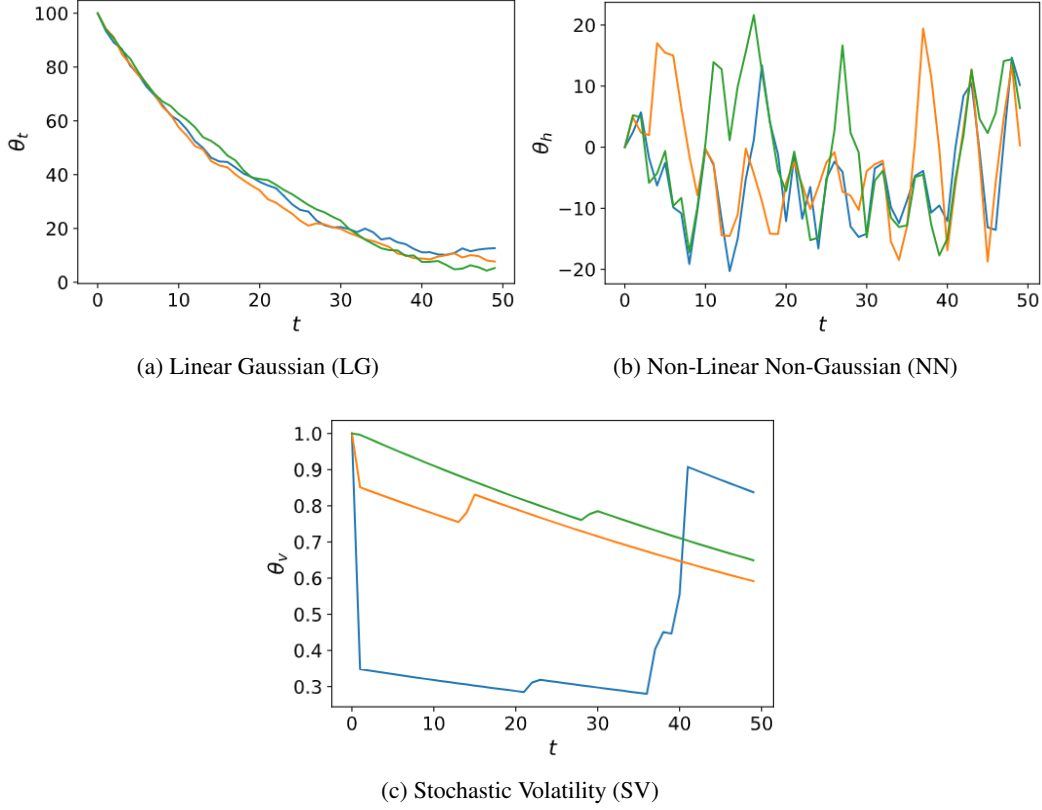


Figure 5: Transition trajectories (different colours) of states (y-axis) sampled from three SSM transition dynamics across 50 time-steps (x-axis) with different random seeds. The complexity of the dynamics gradually increases in SSMs, starting with the smooth LG (a) dynamics, where the difference between consecutive states is very small, followed by NN (b) with more erratic behaviour, and finishing with the SV model (c), whose dynamics has occasional drastic changes of state values.

where $\varepsilon_t \sim \mathcal{N}(0, 1)$; $\theta_\mu = 0$ and $\theta_\beta = 0$ remain the same, while the volatility θ_v follows the transition dynamics, starting with the initial value for the volatility $\theta_{v,0}$ of 1. We set the following priors for LFI of state values: $\theta_\mu \sim \text{Unif}(-2, 2) \in \mathbb{R}$, $\theta_\beta \sim \text{Unif}(-5, 5) \in \mathbb{R}$, $\theta_v \sim \text{Unif}(0, 3) \in \mathbb{R}$.

C Technical Details

C.1 Eye Movement Control for Gaze-Based Selection

An observation model in the gaze selection experiment is a simulated environment, where a human-subject is modelled through a reinforcement learning agent. In this environment, the agent searches for a target on a 2D display, where the target location, actions, observations, and beliefs of the agent are represented by two coordinates $\{c_1, c_2\}$, $c_1, c_2 \in [-1, 1]$ on the display. At each episode of the environment e , the agent receives noisy observations of the target $\mathbf{o}_e = \mathcal{N}(\mathbf{q}, \theta_s \times E^{(e)})$ and moves the gaze to a new location $\mathbf{a}_e = \mathcal{N}(PPO(\mathbf{o}_e, \theta_{om} \times A^{(e)}))$. The beliefs \mathbf{b}_e about the target location \mathbf{q} are updated according to

$$\mathbf{b}_{e+1} = \frac{\sigma_{(o,e+1)}^2 \mathbf{o}_{e+1} + \sigma_{(b,e)}^2 \mathbf{b}_e}{\sigma_{(o,e+1)}^2 + \sigma_{(b,e)}^2}, \quad \sigma_{(b,e+1)} = \sqrt{\frac{\sigma_{(o,e+1)}^2 \sigma_{(b,e)}^2}{\sigma_{(o,e+1)}^2 + \sigma_{(b,e)}^2}}. \quad (15)$$

where $\sigma_{(o,e)}$ and $\sigma_{(b,e)}$ are observation and belief uncertainties respectively, $A^{(e)}$ is the amplitude, and $E^{(e)}$ is the eccentricity of the saccade at the episode e . The user model was trained on 10 000 episodes using the Proximal Policy

Optimization (PPO) algorithm [68], provided by the Stable Baselines3 library [69]. We used default parameters, a multilayer perceptron policy and a clipping parameter set to 0.15. The environment was implemented by Chen et al. [67] in Python with the Open AI gym framework [70].

C.2 UMAP Parameterization

In the UMAP parameterization model, the ground truth for state values is not available, because the human-subject cannot specify the ideal embeddings. Therefore, we approximate the ground truth by using ABC with rejection sampling. Usually, this requires running millions of simulations for each time-step, but we make use of the weighted form of the preference score that allows us to use the same simulations across all time-steps. We simulate 1, 500, 000 embeddings with state values sampled from the prior, and then calculate their corresponding $\mathcal{U}^{(i)}$ and $\mathcal{P}^{(i)}$. For each time-step t , we calculate the preference scores δ and retain only 0.06% of those states that showed the lowest δ values. Finally, we use a Gaussian kernel density estimator (KDE) on the retained state values, and maximize the corresponding PDFs to find the estimations of the ground truth. The bandwidth b of the kernel was calculated according to a Scott’s rule [71] $b = n^{-\frac{1}{d+4}}$, where n is the number of data points and d is the number of dimensions.

The preference score was computed as a weighted sum between the relative validity $\mathcal{U}^{(i)}$ and the classification accuracy $\mathcal{P}^{(i)}$ on the validation set. The relative validity $\mathcal{U}^{(i)}$ is an approximation of the Density Based Cluster Validity (DBCVC) score [62], which is often used as a quality measure of clustering. Intuitively, it shows how separable all the clusters are. We use the HDBSCAN* package [72] and the HDBSCAN Boruvka KDTree [73] algorithm to cluster the points of the embeddings. We set the smallest size grouping to 60, the density parameter of clusters to 10 and leave the rest parameters to their default values. The classification accuracy $\mathcal{P}^{(i)}$ was calculated for the C-Support Vector Classifier (SVC) [63, 64] with the Scikit-learn package [74] and default parameters.

The embeddings for the UMAP parameterization model were computed for the handwritten digit dataset [61]. The dataset was randomly split on the training and validation sets, resulting in 1198 and 599 8x8 pixel images of digits in 10 digit classes. The UMAP algorithm was implemented with the UMAP-learn package [75].

C.3 Implementation Details of Methods

LFI methods from Sections C.3.1-C.3.3 were integrated in the Engine for Likelihood-Free Inference (ELFI) [76] for application and further development.

C.3.1 BOLFI

GP surrogate. The implementation for the GP surrogate was provided by the GPy package [77]. It was initiated with zero mean function, and with the following priors for the RBF kernel lengthscale l , its variance σ_k^2 , and the variance of the bias term σ_b^2 :

$$l \sim \text{Gamma}\left(\frac{\theta_{\max} - \theta_{\min}}{3}, \mathbf{1}\right), \quad \sigma_k^2 \sim \text{Gamma}\left(\frac{\max(\delta^{(i)})^2}{9}, \mathbf{1}\right), \quad \sigma_b^2 \sim \text{Gamma}\left(\frac{\max(\delta^{(i)})^2}{36}, \mathbf{1}\right). \quad (16)$$

where $\theta_{\min}, \theta_{\max}$ are the lower and upper bounds for $\theta^{(i)}$, $(\theta^{(i)}, \delta^{(i)})$ are initial training points, and $\mathbf{1}$ is an all-ones vector. The GP was minimized by using the SCG optimizer [78] on the GP negative log-likelihood with a maximum number of iterations of 50. All inputs $\theta^{(i)}$ for the GP were centred and normalized.

LCBSC acquisition. The BOLFI implementation uses LCBSC [39, 79] as an acquisition function, which chooses points that minimize the lower confidence bound (LCB)

$$\text{LCB}(x) = \mu(x) - \beta_t^{1/2} \sigma(x), \quad \beta_t = 2 \log(t^{2d+2} \pi^2 / 3\delta), \quad (17)$$

where β_t is the confidence parameter, $\delta = 0.1$ is the inverse exploration rate and d is an input dimension.

Posterior sampling. The BOLFI posterior was obtained by weighting the prior samples and using corresponding unnormalized likelihoods as weights

$$p(\mathbf{x}^* | \boldsymbol{\theta}) \propto F\left(\frac{\epsilon - \mu(\boldsymbol{\theta})}{\sqrt{\nu(\boldsymbol{\theta}) + \sigma^2}}\right), \quad (18)$$

with $F(\cdot)$ being a Gaussian CDF with the mean 0 and the variance 1, and where ϵ is the minimum of the GP surrogate mean function $\mu(\cdot)$ obtained by using the L-BFGS-B optimizer [80] with a maximum number of iterations of 1000.

C.3.2 Multi-Objective LFI

LMC surrogate. The LMC model was implemented in BoTorch [81]. Its latent GPs were initialized with linear mean functions $\mu(x) = kx + b$, and RBF kernels. The lengthscales of the kernels were parameterized in log scale, and initialized with 0 along with the constant b of the mean function. For the RBF kernel, ARD was also enabled to assign separate lengthscales for each input dimension. GP latents were also initialized with 50 inducing points uniformly sampled inside the input bounds for each latent GP. The LMC training used Adam optimizer from the tensor computation package PyTorch [82] with a learning rate of 0.1 to minimize the variational evidence lower bound (ELBO). The optimized parameters included LMC coefficients, inducing points locations, and hyperparameters for the mean functions and kernels. We used the default training step size and 1000 epochs for training. All inputs for the LMC were centred and normalized.

qEHVI acquisition. The qEHVI acquisition function used a Quasi-MC sampler [83] with scrambled Sobol sequences [84] and a sample size of 128. The reference point that was used for calculating the hypervolume for each objective was set to -5. The acquisition points were acquired sequentially using successive conditioning [85] with a maximum number of restarts of 20, a batch size limit of 10, and a maximum number of iterations for the optimizer of 200.

Bayesian neural network (BNN) [50] was built from stacked Bayesian layers implemented in torch zoo (BLiTz) [49]. We used an architecture with 2 hidden layers, where each layer had 256 nodes. During the training process, stochastic gradient descent [86] was used with a learning rate of 0.001 for minimizing the ELBO loss with squared L2 norm. The loss was calculated based on 10 samples from the model, for each of 100 batches of training data in a single epoch. The training data was randomly selected from previously stored approximated posterior samples from all states (1000 samples per each state) with replacement, resulting in a total of 1 000 000 points, where one point was a pair of consecutive state values. The training data was updated each time the moving window moved.

Bayesian linear regression (BLR) is defined as $\theta_{t+1} = \theta_t^T \beta + \epsilon$, where $\epsilon \sim N(0, \sigma^2 I)$. The hyperparameters $\sigma \in \mathbb{R}$ and $\beta \in \mathbb{R}^{m \times m}$ were inferred with maximum likelihood estimation (MLE) [87] of

$$p(\theta_{t+1} | \theta_t) \propto \frac{1}{\sigma} \exp - \frac{(\theta_{t+1} - \theta_t \beta)^T (\theta_{t+1} - \theta_t \beta)}{2\sigma^2}. \tag{19}$$

The BLR model was implemented with the probabilistic programming package, PyMC3 [88] that used 100 random samples from three latest inference steps. The pairs (θ_{t-1}, θ_t) and $(\theta_{t-2}, \theta_{t-1})$ pairs were used as inputs for training, and the normal distribution was chosen as a prior family of the BLR parameters. The model was fitted by using the No-U-Turn Sampler (NUTS) [89] with two chains of 2000 samples, 2000 tuning iterations, and a target acceptance rate of 0.85.

Posterior sampling. Similar to BOLFI, the posterior was sampled by using an importance-weighted resampling. Because the main model was implemented in PyTorch, we used the Adam optimizer to learn the threshold ϵ . It used a learning rate of 10^{-4} and 100 optimizing iterations. The optimization started at the parameter point that produced a synthetic observation with the smallest discrepancy.

C.3.3 Sequential Neural Estimators

All three SNEs (SNPE, SNLE and SNRE) and their corresponding surrogate models were implemented in the simulation-based inference [90] and PyTorch [82] packages with default parameters. In all three methods, Adam optimizer with the learning rate of 5×10^{-4} and the training batch size of 50 in 20 epochs were used for training the surrogate. The total gradient norm was clipped in order to prevent exploding gradients at a value of 5.0, and z-score passing was used for surrogate model inputs and outputs.

For **SNPE** [42] and **SNLE** [43], the masked autoregressive flow (MAF) surrogate was used for approximating the posterior $p(\theta | \mathbf{x})$ and likelihood, $p(\mathbf{x} | \theta)$ respectively. The MAF consisted of 5 transformations with 50 hidden features in each of 2 blocks. Each autoregressive transformation had tanh activation along with batch normalization. In contrast, **SNRE** [44] approximates the ratio $\frac{p(\theta, \mathbf{x})}{p(\theta)p(\mathbf{x})}$, where a residual network [91] is used as a classifier trained to approximate likelihood ratios. The goal of the classifier is to predict which of the (θ, \mathbf{x}) pairs was sampled from $p(\theta, \mathbf{x})$ and which from $p(\theta)p(\mathbf{x})$. The residual network had 50 hidden features in 2 residual blocks with 10 (θ, \mathbf{x}) pairs to use for classification.

C.3.4 Recurrent State-Space Models with GP Transitions

In the experiments, we used two variants of recurrent state-space models with GP transitions: **GP-SSM** with a variationally coupled dynamics and trajectories, in which the variational inference scheme for GP transition dynamics is used [53], and probabilistic recurrent state-space model **PR-SSM** [54], which uses doubly stochastic variational inference for efficient incorporation of latent state temporal correlations. Both methods were implemented in the GPT package [53]. The GPs were using Matern32 kernels with linear mean functions, along with 50 randomly sampled inducing points. The number of latent dimensions was set equal to the number of simulator parameters of the observation model. The ELBO loss was calculated from 10 posterior samples and optimized with Adam using a learning rate of 0.001 in 3000 iterations.